

# Application of distributed fiber optic sensing technique in land subsidence monitoring

Jinghong Wu<sup>1</sup> · Hongtao Jiang<sup>2</sup> · Jingwen Su<sup>3,4</sup> · Bin Shi<sup>1</sup> · Yuehua Jiang<sup>3,4</sup> · Kai Gu<sup>1</sup>

Received: 15 January 2015/Revised: 14 July 2015/Accepted: 21 July 2015/Published online: 15 August 2015  
© Springer-Verlag Berlin Heidelberg 2015

**Abstract** Distributed fiber optic sensing (DFOS), a newly developed structure health monitoring technique, has been proved to be a very suitable and useful technique for the monitoring and the early warning of structural engineering. Its application in geotechnical engineering, especially land subsidence resulted by groundwater withdraw, was limited by the complex characteristics of geotechnical materials in the field. In this paper, Brillouin optical time domain reflectometer (BOTDR) and fiber Bragg grating (FBG) techniques were used to monitor the deformation of soil layers and pore water pressure for nearly 2 years in a 200-m borehole with four different types of optical fibers planted directly in the borehole. The result demonstrated that cables with better sheath protection and higher tension strength are more suitable for field monitoring. The main compaction occurs at two thick aquitards which are adjacent to the pumping confined aquifer. The deformation of soil layers shows the conformance with the change of groundwater level over time and the deformation of sand layer had instantaneity while that of clay layer had hysteresis. Rebound amount caused by the rise of ground water level was small, and the re-compression rate significantly decreases after rebounding. This paper demonstrates that

the DFOS technique is a very advanced monitoring method for the investigation on the mechanism of land subsidence and the evaluation of soil compression deformation potential.

**Keywords** Land subsidence monitoring · DFOS technology · Groundwater withdraw · Aquifer system

## 1 Introduction

Due to rapid growths of population and industry demand, large amount of groundwater is being consumed. The extraction of groundwater can generate land subsidence by causing the compaction of susceptible aquifer systems which comprise aquifers and aquitards. Land subsidence has become a worldwide concern since it may cause geological, hydrogeological, environmental, and economic impacts [1–5].

Various ground-based and remote sensing methods have been used to measure and map surface subsidence. Mousavi et al. [6] investigated the land subsidence using 35 GPS stations in the Rafsanjan Plain, Iran, and found 1 m lowering of ground water level may cause ~10–80 mm subsidence. Remote sensing technologies offer advantages, such as large-scale mapping and automation in monitoring the surface displacement. The InSAR techniques are widely used to measure ground displacements associated with groundwater withdrawal [7–9]. Hung et al. [10] used leveling, GPS, multi-level compaction monitoring well, and differential InSAR (DInSAR) to study the extent of subsidence in Taiwan and confirmed that these methods complement each other in spatial and temporal resolutions. However, problems such as high cost, poor precision, and instability of data are always associated with these

✉ Bin Shi  
shibin@nju.edu.cn

<sup>1</sup> School of Earth Sciences and Engineering, Nanjing University, Nanjing 210023, China

<sup>2</sup> School of Geographic and Oceanographic Sciences, Nanjing University, Nanjing 210023, China

<sup>3</sup> Nanjing Institute of Geology and Mineral Resources, Nanjing 210016, China

<sup>4</sup> Nanjing Center, China Geological Survey, Nanjing 210016, China

techniques. Additionally, these techniques generally measure relative changes in the position of the land surface. To better understand the mechanism of subsidence, it is critical to measure compaction at different depths within the aquifer system. Vertical borehole extensometers have been used to measure the continuous change in vertical distance in the interval between the land surface and a reference point or “subsurface benchmark” at the bottom of deep boreholes [11]. Wang et al. [12] analyzed the data of borehole extensometers in Changzhou, China, from 1984 to 2002 and found that the main compressible layer is top aquitard layer of second aquifer. But the measured points of borehole extensometer monitoring system were limited and can only obtain limited deformation information in vertical direction. Its stability and accuracy of measurement are often affected by different factors.

As a new type of sensing technology, distributed fiber optic sensing (DFOS) technology has many unique functions, such as nondestructive capability in distributed monitoring and long-distance monitoring, anti-electromagnetic interference, waterproof, corrosion resistance, durability, etc. By now, DFOS techniques have been successfully applied to many kinds of structural health monitoring, such as tunnels, bridges, concrete piles, pipeline, rock slope, etc. [13–17]. Kunisue and Kikubo [18] illustrated the feasibility of using DFOS in monitoring the deformation of soil layers at different depths in the borehole by laying optical fiber sensors. However, due to the complexity of the characteristics of geotechnical materials in the field, the application of DFOS in monitoring the aquifer system compaction requires more investigation.

In this paper, Brillouin optical time domain reflectometer (BOTDR) and fiber Bragg grating (FBG) techniques were used in a 200-m borehole in Shenze, Suzhou to monitor the deformation of soil layers and pore water pressure in the borehole, respectively. Different types of fiber sensors are planted directly in the borehole to monitor the deformation (micro strains) of the Quaternary sediments and land subsidence for nearly 2 years. Distributed information of soil layer deformation along borehole profile was obtained. On this basis, the mechanism of land subsidence and strata compression was analyzed.

## 2 Working principle

### 2.1 FBG

The principle of operation used in a FBG-based sensor system is to monitor the shift in wavelength of the returned “Bragg” signal with the changes in the Measurand (e.g., strain, temperature). A linear relationship between the strain or temperature and the Bragg wavelength shift has been reported [19, 20]. The Bragg wavelength shift caused by strain can be expressed as

$$\frac{\Delta\lambda_b}{\lambda_b} = c_\varepsilon \Delta\varepsilon, \quad (1)$$

where  $\Delta\lambda_b$  is the change in Bragg wavelength due to variation of strain;  $\lambda_b$  is the original Bragg wavelength under strain free condition;  $\Delta\varepsilon$  is the strain change, and  $c_\varepsilon$  is the calibration coefficient of strain. FBG is one of the quasi-distributed sensing techniques which connects different FBG sensors together in one single fiber to obtain the special discontinuous information at different locations. Based on the monitoring principle, FBG sensors are put into the osmometer cavity. The grating pitch changes when water comes into the cavity and changes the pressure. As a result, the reflected Bragg wavelength has a shift and the pore water pressure can be figured out through a modem.

### 2.2 BOTDR

BOTDR strain sensing technology is based on scattered light which is caused by nonlinear interaction between the incident light and phonons that are thermally excited within the light propagation medium. When this process occurs in an optical fiber, the back-scattered light suffers a frequency shift (the Brillouin frequency) which is dependent on the temperature and strain environment of the fiber [21–23]. It has been found that the frequency shift amount is in proportion to both the longitudinal strain of the optical fiber and its temperature [15]. A significant advantage of Brillouin scattering compared with other scattered light is that its frequency shift caused by temperature is much smaller than that caused by strain (0.002 %/°C). Therefore, while measuring Brillouin frequency shift caused by strain, the influence of temperature on the Brillouin frequency shift can be neglected, if the changes in temperature are within 2 °C [24]. The relationship between Brillouin frequency shift and the optical fiber strain is expressed as

$$v_B(\varepsilon) = v_B(0) + \frac{dv_B(\varepsilon)}{d\varepsilon} \varepsilon, \quad (2)$$

where  $v_B(\varepsilon)$  is the Brillouin frequency under the strain  $\varepsilon$ ,  $v_B(0)$  is the Brillouin frequency shift without stain;  $\frac{dv_B(\varepsilon)}{d\varepsilon}$  is strain coefficient and the proportional coefficient of strain at a wavelength of 1.55  $\mu\text{m}$  is about 0.5 GHz/ % (strain). According to this relationship, strain distributed along the sensing optical fiber can be measured.

## 3 Laboratory tests about coupling effects

### 3.1 Coupling effect between the soil and the coupling materials

A series of experiments have been done on different coupling materials in order to improve the deformation

compatibility of the sensing fibers with the surrounding in situ soil. The results show that the volume of bentonite expands after absorbing the water. Sand and gravel are then extruded all around due to the expansion of the bentonite which makes the serum better filling in the cracks or fissures as well as increases the coupling effect of the slurry and the soil. The strength of the consolidation samples are primarily affected by the ratio of sand–gravel to bentonite. According to the experimental data of the in situ undisturbed soil, the optimum mixture ratio of the sand–gravel–bentonite is obtained. This coupling material can meet the requirements of mobility for field operation and its mechanical features are almost consistent with those of in situ soil to ensure a better coupling effect of the surrounding soil and the sand–gravel–bentonite.

### 3.2 Coupling effect between coupling materials and the fiber sensors

The coupling performance between the sand–gravel–bentonite and the sensors are studied based on the pullout test. The pullout test device is shown in Fig. 1. Curing time, confining pressure, and the type of optical fiber are considered as the main factors which determine the friction resistance of fiber-coupling material interface. By studying the friction resistance, the coupling effect is analyzed. Fibers with different sheaths are tested around different confining pressures (0, 30, and 60 kPa) in sand–gravel–bentonite samples of different curing times (7, 14, and 28 days). The results show that the drawing friction resistance of fiber-coupling material interface increases with increasing curing time and increasing confining pressures. However, there is no special relationship between the types of fibers and the drawing friction resistance of fiber-coupling material interface [25].

Strain transfer from the sand–gravel–bentonite to the fiber sensors is a key which determines the land subsidence monitoring accuracy. According to the laboratory test, the initial strain value is collected 30 days after filling the

sand–gravel–bentonite in order to increase the consolidation time. Meanwhile, under the huge confining pressure within the borehole it is considered that there is a good coupling effect of the fiber sensors and the sand–gravel–bentonite in the field. Hence, the strain monitored can make a real response to the strain of the soil layers.

## 4 DFOS-based land subsidence monitoring scheme

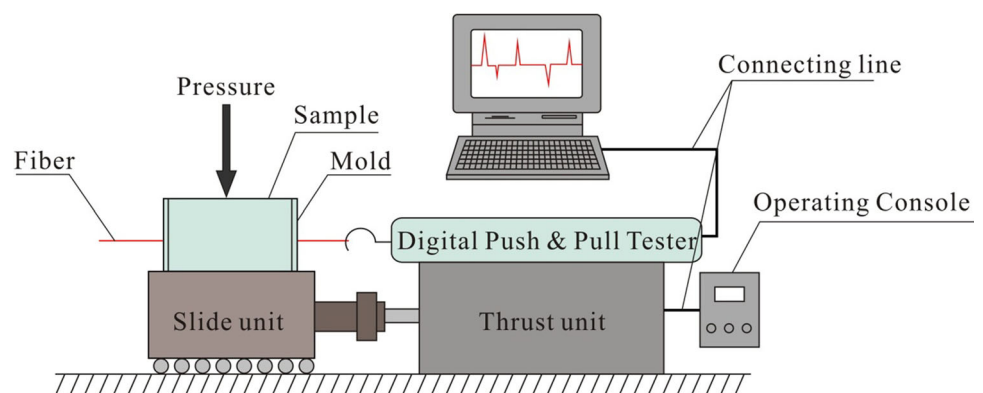
### 4.1 Strata distribution in the borehole

Suzhou is located at the lower reaches of the Yangtze River in southeastern Jiangsu, China (Fig. 2), where Quaternary sediments are widely distributed with multilayer clayey soils and loose sand layers exist alternately [26–28]. According to the intensive exploitation of groundwater, this area has suffered from severe land subsidence in the past several decades. Shenze, in the south of Suzhou, is a typical area where the yearly land subsidence reached 54 mm in 2007 [29]. To monitor the compression of different soil layers at different depths, a 200-m borehole was drilled in this area ( $30^{\circ}53'23.96''\text{N}$ ,  $120^{\circ}40'47.11''\text{E}$ ). The quaternary multilayer aquifer system can be divided into three groups (Group I, II, and III), including three confined aquifers and four aquitards, see Table 1.

### 4.2 Fibers and equipment

Four types of fiber sensors supplied by Suzhou NanZee Sensing Ltd, China were used in this project. Three 900  $\mu\text{m}$ -diameter strain sensing fibers are coated by polyurethane, metal reinforcers, and steel conduit, named polyurethane sheath cable (PSC), metal-reinforced cable (MRC) and 10-m fixed-point cable (FPC). PSC and MRC are tight-buffered, while FPC is tight-buffered only at the fixed points which are fixed with a 5-mm inner-diameter metal aluminum tube and a 10 cm-long heat shrinkage tube

**Fig. 1** Pullout test device



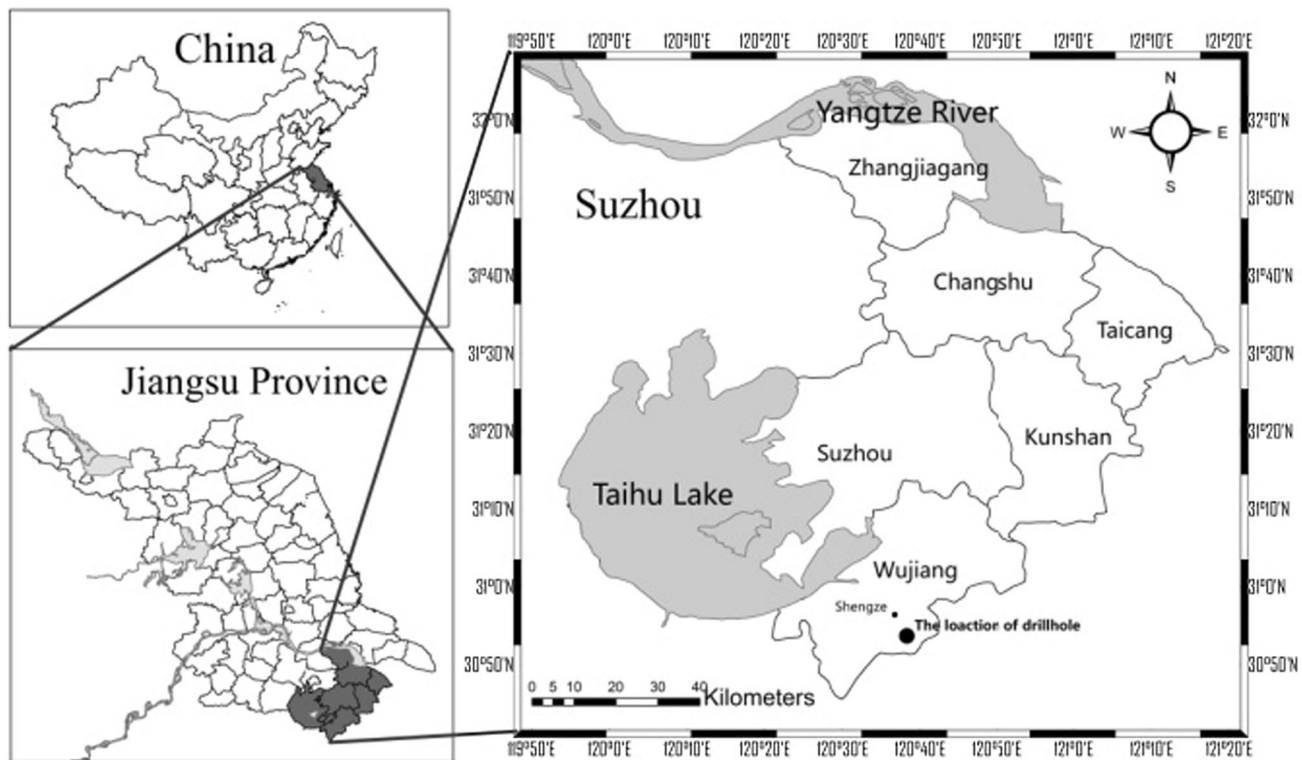


**Fig. 2** Location of Suzhou City and the study borehole

**Table 1** Division of aquifer groups

Geologic time	Burial depth (m)	Aquifer groups		Soil type
		Group	Layer	
Qh	0–5.3		Cover layer	
Qp <sub>3</sub>	5.3–37.0	Group I	Aquitard I (Ad1)	Clay
	37.0–41.2		Aquifer I (Af1)	Silty-fine sand
Qp <sub>2</sub>	41.2–74.35	Group II	Aquitard II (Ad2)	Clay, silt
	74.35–87.7		Aquifer II (Af2)	Fine-medium sand
Qp <sub>1</sub>	87.7–137.9	Group III	Aquitard III (Ad3)	Slay, silt, clay with fine sand
N <sub>2</sub>	137.9–151.0		Aquifer III (Af3)	Fine-medium sand
	151.0–165.1	Group IV	Aquitard IV (Ad4)	Silt, clay with fine sand
N <sub>1</sub>	165.1–200.0		Consolidation layer	Consolidation

by epoxy resin. The structures of these three types of fiber sensors are shown in Fig. 3. MRC, which can effectively protect the optical fibers with several metal reinforcers, has good coupling and uniformity with soil by the screw structure of the sensor surface (Fig. 3b). FPC, with unique fixed-point design, can be used to measure spacial inhomogeneous and discontinuous section (Fig. 3c). The BOTDR analyzer used in this study is N8511 Optical Fiber Temperature/Strain Analyzer produced by ADVANTEST Co. Ltd, Japan. Its minimum spatial resolution is 1 m, the readout resolution accuracy is 5 cm and the strain measurement accuracy is about  $\pm 40\mu\epsilon$ . The FBG interrogator

used is SM125 FBG interrogator produced by Micron Optics International Co. Ltd, America. SM125 is a kind of full spectrum measurement equipment with a precision of 1 pm.

### 4.3 Monitoring scheme

As shown in Fig. 4, a borehole, 200 m in depth and 129 mm in diameter, was drilled for DFOS monitoring. During the installation process, a 15 kg guide hammer was used to drag the four sensing fibers down to the borehole bottom. The descending speed of the guide hammer was

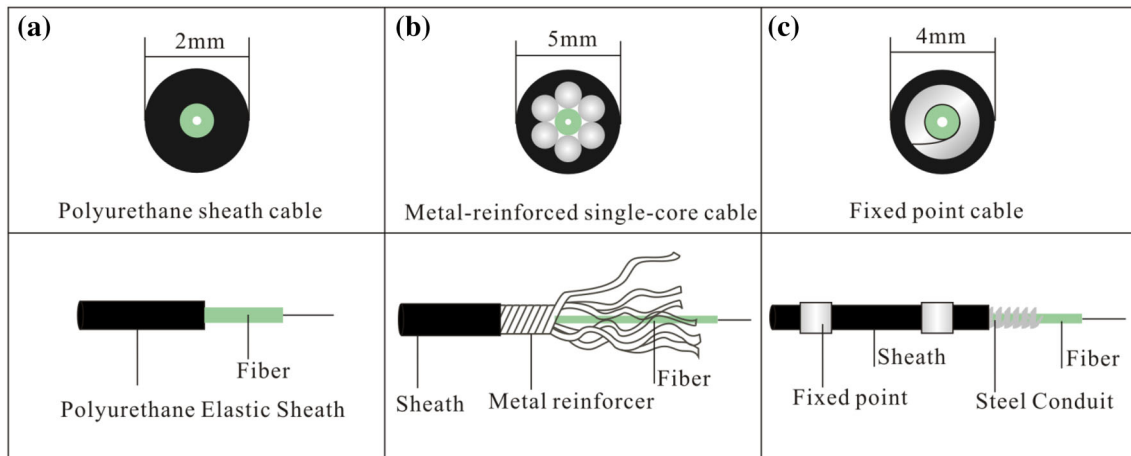


**Fig. 3** Schematic illustration of the structures of strain sensing fibers. **a** Section diagram of PSC. **b** Section diagram of MRC. **c** Section diagram of FPC

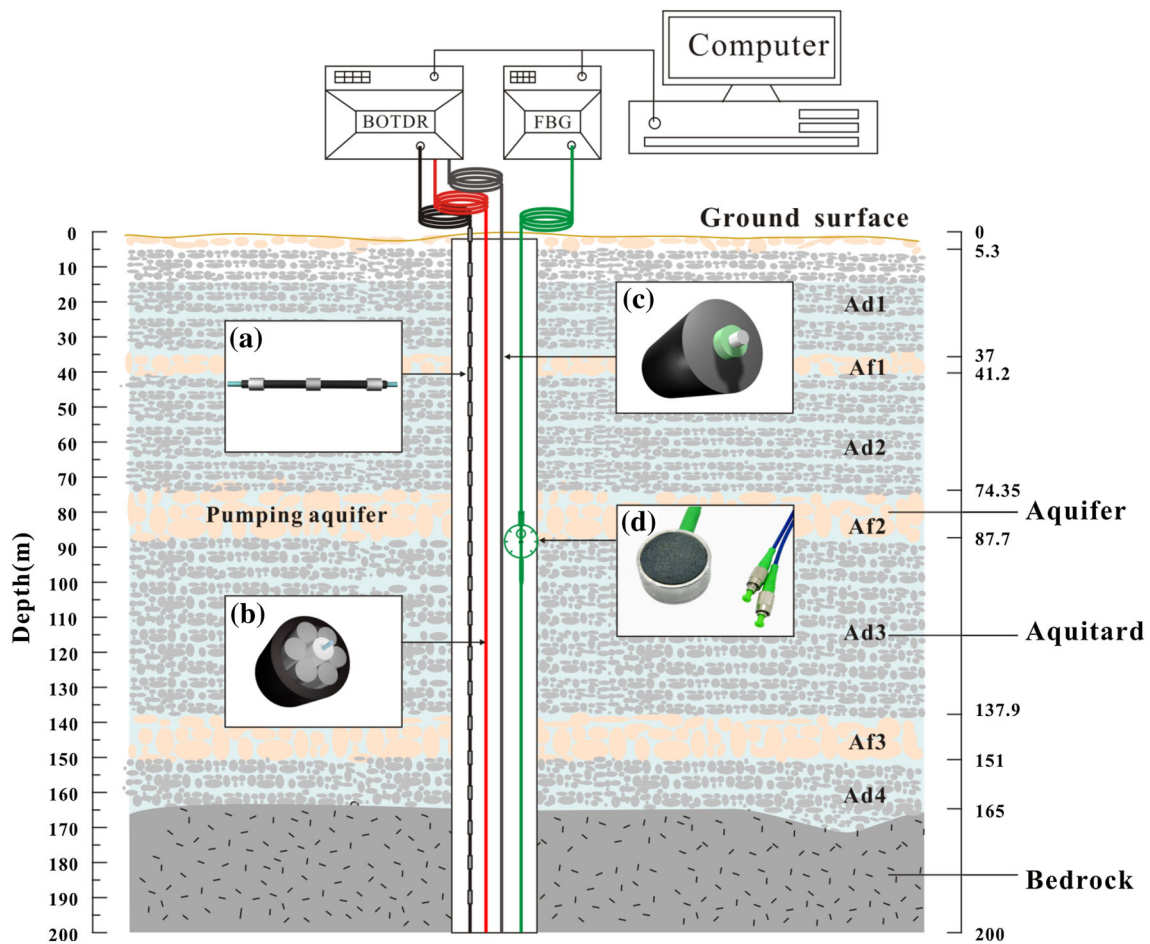


**Fig. 4** Layout of the sensing fibers in the drilling hole; **a** 10-m fixed-point cable; **b** metal-reinforced cable; **c** polyurethane sheath cable; **d** FBG mini-osmometer

controlled by being tied with a wire rope. The strain sensing fibers were monitored with BOTDR to obtain the deformation of the aquifer system (see Fig. 4a–c). The

sampling interval is 5 cm. Additionally, a FBG-based mini-osmometer was embedded at the depth of 87.7 m to measure the pore water pressure of the main pumping

aquifer (see Fig. 4d). The borehole was filled with fine sand–gravel–bentonite tested in the laboratory after the sensors being installed. The optimum mixture ratio of the sand–gravel–bentonite was obtained according to the experimental data of the in situ undisturbed soil.

Generally, temperature sensing fibers are needed to lay together with the strain sensing fibers in order to minus the influence of temperature. However, it is worth noting that the geothermal field is almost constant in the deep soil [30], so that the influence of temperature can be ignored in this case. The DFOS monitoring system was built on November 25, 2012. The initial data were collected 1 month later on December 25 and the monitoring was carried out in the next two years until November 17, 2014.

### 5 Results and discussion

#### 5.1 Strain monitoring using different sensing fibers

Three types of sensing fibers were pre-stretched and embedded in the borehole for strain monitoring. The strain distributions of the sensing cables on December 25, 2012 are plotted in Fig. 5. It can be seen that PSC had bigger fluctuation than the other two cables due to its small stiffness. The data missing below 150 m indicated the breakage of the fiber due to its low tensile strength. By contrast, MRC and FPC had enough stiffness and tensile strength due to the protection of metal reinforcers and steel conduit to maintain the stability under complex conditions. Moreover, pre-tensioning effect of MRC is not obvious. FPC can measure the strain only between adjacent two points without strain share on the fiber hence it has the best accuracy in measuring the strain [31].

To better understand the strain loss of different optical fiber sensors, tensile tests have been done for the FPC and MFC. The cable ends were fixed on the tensile test device (Fig. 6). The deformation which was controlled by the dial gage reading was added step by step. The cable strain was monitored by BOTDA and the dial gage reading was recorded at each step. The dial gage reading is on behalf of the actual displacement while the monitored displacement can be calculated by Eq. (3) using the strain monitored by BOTDA.

$$\Delta D = \int_{h_1}^{h_2} \varepsilon(h)dh, \tag{3}$$

where  $\Delta D$  is the elongation or compression from  $h_1$  to  $h_2$ ;  $\varepsilon(h)$  is the strain along the depth. The calculation results of FPC and MRC are shown in Fig. 7. The monitored displacements of FPC (Fig. 7a) and MRC (Fig. 7c) at each step are smaller than the actual displacement because of the

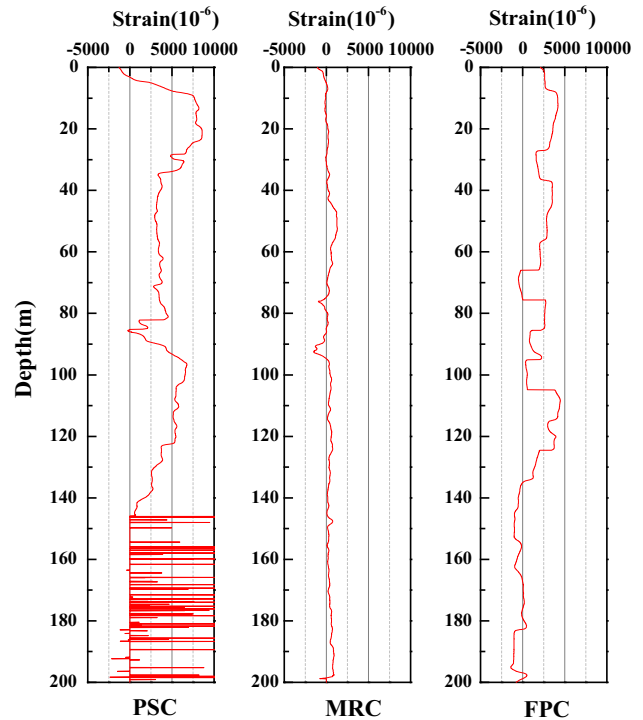


Fig. 5 Initial strain distributions of three cables within 200 m depth

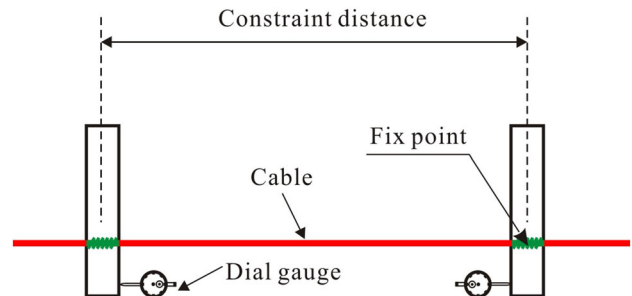


Fig. 6 Schematic diagram of tensile test

strain loss results from the sheathes. With the increase of tensile level, absolute error between the monitored displacement and the actual displacement of FPC reduces. On the contrary, absolute error of MRC increases gradually with the increasing tensile level. The average relative errors of FPC and MRC are 3.66 and 5.27 %, respectively. According to the Eq. (4), the strain loss

$$I = \frac{\varepsilon_A - \varepsilon_M}{\varepsilon_A} \times 100 \%, \tag{4}$$

is obtained where  $\varepsilon_A$  is the actual strain,  $\varepsilon_M$  is the monitored strain,  $I$  is strain loss. The relationship between the strain loss and the actual displacement is shown in Fig. 7b, d. It can be seen that with the increasing displacement the strain loss of FPC decreases. There is almost no loss when displacement reaches 60 mm. For the MRC, strain loss

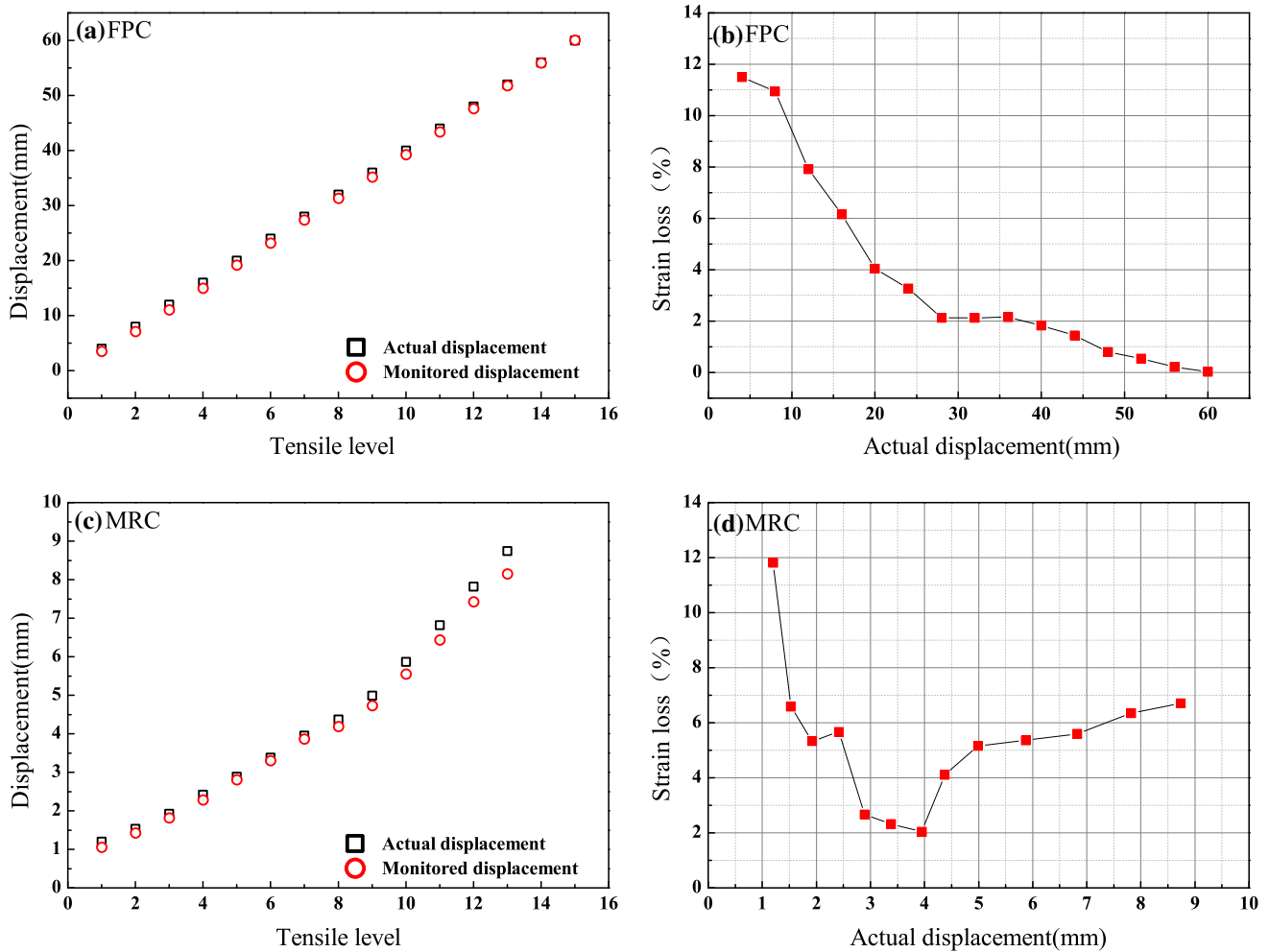


Fig. 7 Calibration test of FPC and MRC

decreases obviously with the increasing displacement (0–4 mm) and then increases generally. The average strain losses of FPC and MRC are 3.67 and 5.36 %, respectively.

**5.2 Deformation characteristics of main compression layers**

The data obtained on December 25, 2012 were set as the initial data and were subtracted from the latter monitoring data. The strain distributions on different dates are plotted in Fig. 8. PSC and 10 m-FPC show large negative strain from ground surface to 10 m in depth, while MRC shows the positive strain. These abnormal strains are attributed to the frequent fluctuation of shallow soil temperature. The three cables show the similar variation below 10 m, that is, significant negative strains were obtained at the depths of 42.35–74.35 and 87.7–111.5 m. The negative strain increased with time demonstrating that Ad2 and Ad3, which are close to the pumping aquifer Af2, were the main compression strata. In addition, the compression induced

by groundwater withdrawal was uneven in the vertical direction. The shorter the distance between the aquitard and the pumping aquifer, the greater the degree of compression of the aquitard.

Strain is integrated along the depth for the elongation or compression which indicates the deformation of soil layers. Deformation over time curve of three cables from 41.2 to 137.9 m, that is from Ad2 to Ad3, can be calculated through Eq. (3). Figure 9 illustrates the deformation variations of three sensing fibers over time. As show in Fig. 9, the process of deformation can be divided into three stages. Before September 30, 2013, the soil layer was compressed (Stage I). After that, there was a small rebound of soil layers (Stage II). Since March 9, 2014, the compression of soil layer (from Ad2 to Ad3) has been observed again and it increased constantly.

Table 2 summarizes the deformation characteristics of three stages using different strain sensing cables. It was found that the compression deformation of three cables shows the tendency of PSC > FPC > MRC at both stage I

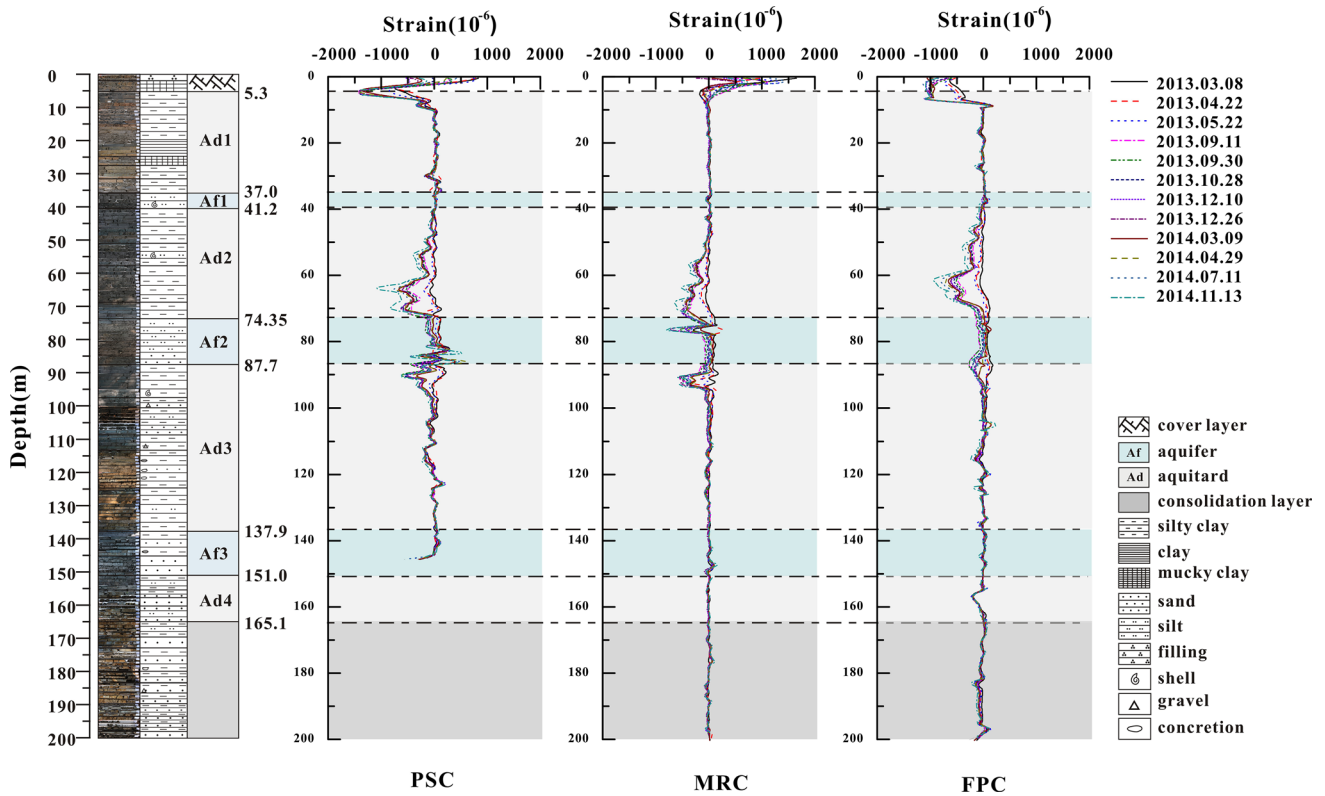


Fig. 8 Drill core profile and strain distributions of three cables within 200-m depth

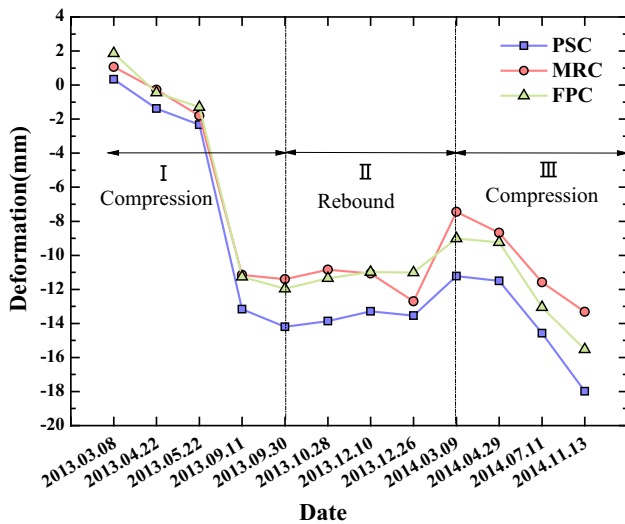


Fig. 9 Deformation–history curves of soil layer from Ad2 to Ad3

and III. The rebound deformation shows the tendency of  $MRC > PSC > FPC$  at stage II. The difference between the deformations measured by different optical fibers is due to their different strain transfer coefficients, which is affected by the length of the sensor, the thickness and Young’s modulus of the interlayer. It has been reported that the average strain transfer coefficient increases with sensor

length, rises with the increase of the interlayer Young’s modulus, and decreases with the thickening of the interlayer [32, 33]. PSC has the smallest strain loss but it is easier to have a breakpoint due to the lack of sheath protection. FPC has less strain loss and higher precision for strain monitoring than MRC, although MRC has the biggest Young’s modulus (i.e., 5.4 GPa, bigger than 1.9 GPa of FPC and 0.3 GPa of PSC). It was also observed that the rebound deformation was only about 21–34.6 % of the compression deformation, illustrating plastic deformation of soil layer. The compression rate at stage I ranged from 1.23 to 1.53 mm/month and ranged from 0.71 to 0.81 mm/month at stage III. The re-compression rate decreases more than a half compared with the previous compression. If this compression-rebound cycle continues, the compression rate may become more and more slow and land subsidence may possibly enter into the stage of “die” no matter whether there is ground water pumping or not.

### 5.3 Relationship between groundwater withdrawal and aquifer system compaction

FPC was taken for the detailed analysis of aquifer system compaction because of its high accuracy in strain monitoring. Figure 10a, b illustrates the deformation variation of the aquifers (Af1, Af2, and Af3) and the aquitards (Ad1,



**Table 2** Deformation characteristics of different stages using different cables

Cable type	Stage I		Stage II		II/I (%)	Stage III		
	Compression (mm)	Rate (mm/month)	Rebound (mm)	Rate (mm/month)		Compression (mm)	Rate (mm/month)	Rate III/I (%)
PSC	-14.21	1.53	+2.98	0.56	21.0	-6.76	0.81	53.1
MRC	-11.40	1.23	+3.95	0.74	34.6	-5.87	0.71	57.5
FPC	-11.97	1.30	+2.95	0.55	24.6	-6.50	0.78	60.7

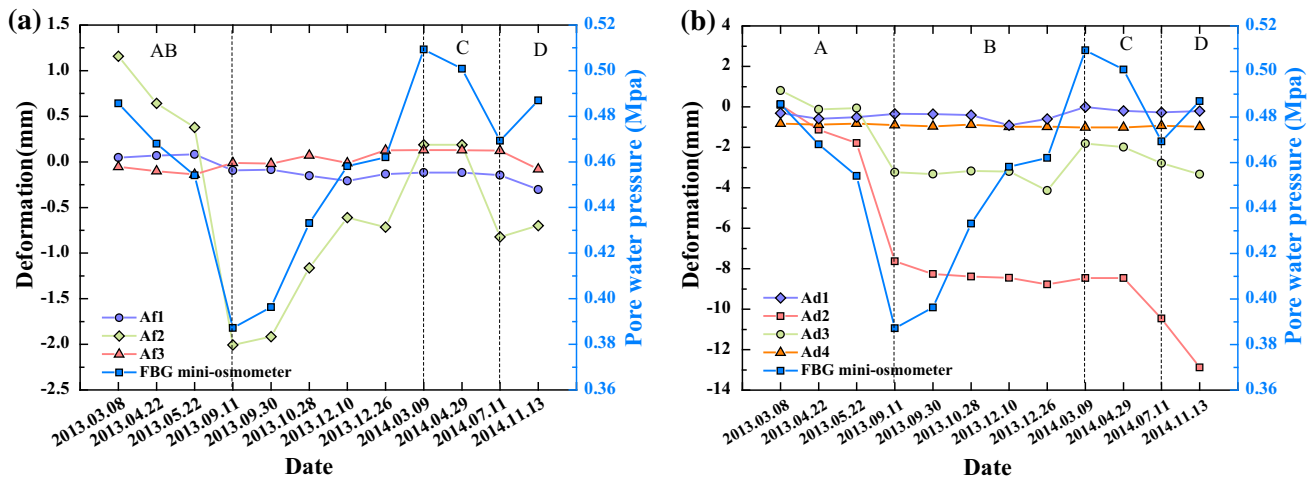


**Fig. 10** Deformation–history curves of soil layers. **a** Relationship between deformation of three aquifers and the pore water pressure of Af2. **b** Relationship between deformation of the three aquitards and the pore water pressure of Af2

Ad2, Ad3, and Ad4), respectively. Pore water pressure change of Af2 obtained by FBG mini-osmometer was also plotted in Fig. 10a, b. As can be seen, the pore water pressure decreased during period A and increased during period B, then re-decreased during period C and re-increased during period D. This was attributed to the larger consumption of groundwater in the summer than in the winter.

In Fig. 10a, Af1 and Af3 have little deformation while the deformation of Af2 shows a good consistency with pore water pressure, indicating that the pumping aquifer Af2 is the main deformation sand layer. In Fig. 10b, however, no significant deformation of Ad1 and Ad4 was observed. Since Ad1 had a small overlying pressure, it is unlikely to be compressed under overlying pressure with small variation. Ad4 is found to almost consolidate into rock according to soil samples. Ad2 and Ad3 are the main compressed clay layers, agreeing well with Fig. 8. The comparison between Fig. 10a, b indicates that unlike the deformation of sand layer there is a lag effect existing between the deformation, and the groundwater level changes because of the low permeability of clayey soil layer. In addition, the rebound percentage of clay layer was much smaller than that of sand layer, indicating that sand

layer has good elasticity while plastic deformation of clay layer can not be ignored. Aquitards often contain interlayer with high permeability, such as silt and clay-like loam which lead to large compression deformation while pumping, and the deformation is often irreversible.

## 6 Conclusions

This paper presents a new in situ monitoring method for the amount of stratified compaction in boreholes drilled several hundred meters underground. Different sensing fibers are applied to monitor aquifer system deformation. Successful monitoring using DFOS-based method is expected to enable a quantified evaluation of ground compaction associated with groundwater withdrawal. Several conclusions can be drawn from the monitoring data:

1. The results show that the DFOS is a very advanced technique for monitoring the soil subsidence due to its incomparable function of distributed monitoring. From the monitoring results, strain changes at any depth of the soil layers can be seen while this cannot be realized by other traditional systems. DFOS technique can

effectively reflect the vertical deformation of aquifer system and can be used in land subsidence monitoring and early warning.

2. PSC is unsuitable for deep monitoring of land subsidence due to its small stiffness, while MRC and 10-m FPC have a better monitoring effect.
3. Land subsidence in Suzhou mainly occurs from 41.35 m to 111.5 m depth, where the two aquitards adjacent to the pumping aquifer are found. In addition, compression induced by groundwater withdrawal is uneven in the vertical direction. The shorter the distance between the aquitard and the pumping aquifer, the greater the degree of compression of the aquitard.
4. Even if the ground water level recovers, there is only about 21–34.6 % rebound that occurs in the main compression layer. The re-compression rate decreases more than a half compared with the previous compression rate. If this compression-rebound cycle continues, there may no longer be compression of the soil layer. The monitoring work will be continued to investigate the re-compression rule.
5. The deformation mechanism of sand layer and clay layer is different. Sand layer has a good elasticity while plastic deformation of clay layer exists during pumping process. Sand layer deformation has the characteristic of instantaneity, while clay layer usually lags because of the low permeability.

**Acknowledgments** The authors gratefully acknowledge the financial support provided by the State Key Program of National Natural Science of China (Grant No. 41230636), the National Natural Science Foundation of China (No. 41372265), the National Land and Resources Survey (No. 1212010914006), and the Evaluation of Geology and Mineral Resources Survey (No. 1212011220002). The authors would also like to thank the technical staff of the Suzhou NanZee Sensing Ltd for their assistance in the developing of the optical fibers.

## References

1. Phien-wej N, Giao PH, Nutalaya P (2006) Land subsidence in Bangkok, Thailand. *Eng Geol* 82:187–201. doi:10.1016/j.enggeo.2005.10.004
2. Pacheco-martínez J, Hernandez-marín M, Burbey TJ et al (2013) Land subsidence and ground failure associated to groundwater exploitation in the Aguascalientes Valley, México. *Eng Geol* 164:172–186. doi:10.1016/j.enggeo.2013.06.015
3. Holzer TL, Johnson AL (1985) Land subsidence caused by ground water withdrawal in urban areas. *GeoJournal* 11:245–255
4. Chen XX, Luo ZJ, Zhou SL (2014) Influences of soil hydraulic and mechanical parameters on land subsidence and ground fissures caused by groundwater exploitation. *J Hydrodyn* 26:155–164. doi:10.1016/S1001-6058(14)60018-4
5. Hung WC, Hwang C, Liou JC et al (2012) Modeling aquifer-system compaction and predicting land subsidence in central Taiwan. *Eng Geol* 147–148:78–90. doi:10.1016/j.enggeo.2012.07.018
6. Mousavi SM, Nagr MH, Shamsai S (2000) Application of GPS to evaluate land subsidence in Iran. In: Proceedings of the Sixth International Symposium on Land Subsidence, Ravenna, Italy, pp 107–112
7. Hooper A, Zebker H, Segall P, Kampes B (2004) A new method for measuring deformation on volcanoes and other natural terrains using InSAR persistent scatterers. *Geophys Res Lett*. doi:10.1029/2004GL021737
8. Galloway DL, Hudnut KW, Ingebritsen SE et al (1998) Detection of aquifer system compaction and land subsidence using interferometric synthetic aperture radar, Antelope Valley, Mojave Desert, California. *Water Resour Res* 34:2573–2585
9. Jiang LM, Lin H, Ma JW et al (2011) Potential of small-baseline SAR interferometry for monitoring land subsidence related to underground coal fires: Wuda (Northern China) case study. *Remote Sens Environ* 115:257–268. doi:10.1016/j.rse.2010.08.008
10. Hung WC, Hwang C, Chang CP et al (2010) Monitoring severe aquifer-system compaction and land subsidence in Taiwan using multiple sensors: Yunlin, the southern Choushui River Alluvial Fan. *Environ Earth Sci*. doi:10.1007/s12665-009-0139-9
11. Riley FS (1969) Analysis of borehole extensometer data from central California. *Land Subsid* 2:423–431
12. Wang GY, Yu J, Wu SL, Wu JQ (2009) Land subsidence and compression of soil layers in Changzhou area. *Geol Explor* 45:612–620
13. Zhu HH, Shi B, Yan JF et al (2014) Fiber Bragg grating-based performance monitoring of a slope model subjected to seepage. *Smart Mater Struct* 23:1–12. doi:10.1088/0964-1726/23/9/095027
14. Li HN, Li DS, Song GB (2004) Recent applications of fiber optic sensors to health monitoring in civil engineering. *Eng Struct* 26:1647–1657. doi:10.1016/j.engstruct.2004.05.018
15. Wang BJ, Li K, Shi B, Wei GQ (2009) Test on application of distributed fiber optic sensing technique into soil slope monitoring. *Landslides* 6:61–68. doi:10.1007/s10346-008-0139-y
16. Gao JQ, Shi B, Zhang W et al (2005) Application of Distributed Fiber Optic Sensor to Bridge and Pavement Health Monitoring. *J Disaster Prev Mitig Eng* 23:14–19
17. Zhu HH, Shi B, Zhang J et al (2014) Distributed fiber optic monitoring and stability analysis of a model slope under surcharge loading. *J Mt Sci* 11:979–989. doi:10.1007/s11629-013-2816-0
18. Kunisue S, Kokubo T (2010) In situ formation compaction monitoring in deep reservoirs using optical fibres. *IAHS-AISH, Wallingford*, pp 368–370
19. Kersey AD, Davis MA, Patrick HJ et al (1997) Fiber grating sensors. *J Light Technol* 15:1442–1463. doi:10.1109/50.618377
20. Zhu HH, Yin JH, Zhang L et al (2010) Monitoring internal displacements of a model Dam using FBG sensing bars. *Adv Struct Eng* 13:249–262. doi:10.1260/1369-4332.13.2.249
21. Bao X, Dhliwayo J, Heron N et al (1995) Experimental and theoretical studies on a distributed temperature sensor based on Brillouin scattering. *J Lightwave Technol* 13:1340–1348
22. Horiguchi T, Kurashima T, Tateda M (1989) Tensile strain dependence of Brillouin frequency shift in silica optical fiber. *IEEE Photonics Technol Lett* 1:107–108
23. Horiguchi T, Kurashima T, Koyamada Y (1993) Measurement of temperature and strain distribution by Brillouin frequency shift in silica optical fibers. *Fibers* 92. *Int Soc Opt Photonics* 1797:2–13
24. Zhang D, Shi B, Cui HL, Xu HZ (2004) Improvement of spatial resolution of Brillouin optical time domain reflectometer using spectral decomposition. *Opt Appl* 34:291–302

25. Yang H, Zhang D, Shi B et al (2012) Experiments on coupling materials' proportioning of borehole grouting in directly implanted optic fiber sensing. *J Disaster Prev Mitig Eng* 32:714–719
26. Jiang HT, Wang FB, Yang DY (2003) A study on Paleo-geography of late quaternary and engineering geological condition of Suzhou urban district. *Sci Geogr Sin* 23:82–86
27. Jiang HT, Shi B (1995) Study on the engineering geological properties of shallow layer in Suzhou city. *Hydrogeol Eng Geol* 22:35–37
28. Li CX, Fan DD, Zhang JQ (2000) Late quaternary stratigraphical framework and potential environmental problems in the Yangtze Delta area. *Mar Geol Quat Geol* 20:1–8
29. Land and Resources of Jiangsu Province (2007) Land subsidence monitoring report of Su-Xi-Chang area. Land and Resources of Jiangsu Province, Shanghai
30. Wu JH, Tang CS, Shi B et al (2014) Effect of ground covers on soil temperature in urban and rural areas. *Environ Eng Geosci* 20:225–237
31. Lu Y, Shi B, Xi J et al (2014) Field study of BOTDR-based distributed monitoring technology for ground fissures. *J Eng Geol* 22:8–13
32. Van Steenkiste JR, Kollar LP (1998) Effect of the coating on the stresses and strains in an embedded fiber optic sensor. *J Compos Mater* 32:1680–1711
33. Li QB, Li G, Wang GL (2003) Effect of the plastic coating on strain measurement of concrete by fiber optic sensor. *Measurement* 34:215–227